

Check for updates

AI-Driven Robot Enables Synthesis-Property Relation Prediction for Metal Halide Perovskites in Humid Atmosphere

Ansuman Halder, Maher B. Alghalayini, Shuan Cheng, Nikil Thalanki, Thong M. Nguyen, Abigail R. Hering, Do-Kyoung Lee, Simon Arnold, Marina S. Leite, Edward Barnard, Aleksandr Razumtcev, Morgan Wall, Arian Gashi, Yi-Ru Liu, Marcus M. Noack, Shijing Sun,* and Carolin M. Sutter-Fella*

Materials Acceleration Platforms (MAPs) - also known as self-driving laboratories- present a new paradigm for materials science and promise an order of magnitude accelerated materials discovery compared to the traditional trial-and-error approach. Metal halide perovskites (MHPs) are an emerging class of materials for optoelectronic applications but are plagued by irreproducible optoelectronic quality, particularly for films fabricated in a humid atmosphere. Here, a machine learning (ML)-guided closed-loop platform is developed with a multimodal data fusion approach to predict synthesis-property relations for the optical quality of MHP thin films in relative humidities (RHs) ranging from 5-55%. The efficiency of this approach is confirmed by the fast-dropping learning rate to 2% after experimentally sampling less than 1% of the possible 5,000+ combinations. The prediction of synthesis-property relations is done by optical and imaging characterizations. In situ photoluminescence characterization revealed the origin of thin film quality variation at different RH. These insights provide an avenue for controlling the MHP crystallization by fine-tuning the synthesis parameters and RH for a given chemistry, thus lifting the need for stringent atmosphere control. The MAP enables an accelerated screening and understanding of the synthesis design space, facilitating rational synthesis recipe choice for a wide range of materials.

1. Introduction

Traditionally, materials discovery has been a time-consuming, expensive effort based on intuition and the Edisonian trial-and-error experimentation approach. Fueled by advanced computation, artificial intelligence (AI), and robotics, Materials Acceleration Platforms (MAPs) are an emerging paradigm in materials science to accelerate materials optimization discovery.[1] MAPs-also known as self-driving laboratoriesautomate the materials discovery process by building a closed-loop workflow that integrates synthesis, characterization, robotics, and machine learning (ML) algorithms.[2-7] The Mission Innovation report stated that MAPs "envisage(s) a Moore's law for research, where the rate of research doubles every two years."[1] MAPs hold the promise to accelerate the discovery of materials and clean energy innovations by a factor of ten, i.e., from 10–20 years to 1–2 years. [1,8] The success

A. Halder, M. B. Alghalayini, N. Thalanki, D.-K. Lee, S. Arnold, E. Barnard, A. Razumtcev, M. Wall, A. Gashi, Y.-R. Liu, C. M. Sutter-Fella Molecular Foundry

Lawrence Berkeley National Laboratory

Berkeley, CA 94720, USA E-mail: csutterfella@lbl.gov

M. B. Alghalayini Energy Storage and Distributed Resources Lawrence Berkeley National Laboratory Berkeley, CA 94720, USA

M. B. Alghalayini, M. M. Noack Applied Mathematics and Computational Research Division Lawrence Berkeley National Laboratory

Lawrence Berkeley National Laborator Berkeley, CA 94720, USA

The ORCID identification number(s) for the author(s) of this article can be found under https://doi.org/10.1002/aenm.202502294

DOI: 10.1002/aenm.202502294

S. Cheng, S. Sun
Department of Mechanical Engineering
University of Washington
Seattle, WA 98195, USA
E-mail: shijing@uw.edu
T. M. Nguyen

T. M. Nguyen
Paul G. Allen School of Computer Science & Engineering
University of Washington
Seattle, WA 98 195, USA
D.-K. Lee

Nevada Extreme Conditions Laboratory University of Nevada Las Vegas, NV 89154, USA A. R. Hering, M. S. Leite Department of Materials Science and Engineering University of California 1 Shields Ave, Davis, CA 95616, USA



16146840, 0, Downloaded from https://advanced.onlinelibray.wiley.com/doi/10.1002aenn...0292294 by University Of California - Davis, Wiley Online Library on [1607/2025]. See the Terms and Conditions (https://onlinelibrary.wiley.com/terms-and-conditions) on Wiley Online Library for rules of use; OA articles are governed by the applicable Creative Commons Licenses

of MAPs was demonstrated for various multidisciplinary materials science questions in recent years. For example, Ceder et al. reported 41 inorganic powder compounds proposed by natural-language models within 17 days of continuous operation. [5] Cronin et al. demonstrated that a curiosity algorithm robot revealed properties of unfamiliar systems that would not have been possible with the same budget (time, cost) using a random parameter search. [9] Brabec et al. reported the efficient optimization of multicomponent polymer blends for organic photovoltaics with almost 100 times smaller materials consumption used in autonomous experiments compared to the manual process. [10]

Here, metal halide perovskites (MHPs) such as the formamidinium lead iodide (FAPbI₃) family are chosen as a model system because they are infamously known for their sensitivity to relative humidity (RH), leading to instability and irreproducible film formation. The exact synthesis parameters (e.g., antisolvent drop time, annealing temperature, annealing time, atmosphere) and their combinatorial interplay affect film quality reproducibility. In this regard, robotic platforms are highly suited for a systematic parameter screening as demonstrated by Zhang et al.[11] Stringent requirements on the fabrication atmosphere significantly increase the complexity and cost of the fabrication processes. It was found that the presence of RH during film formation can lead to uncontrollable crystallization as well as phase instability.[12] On the other hand, Eperon et al. showed that RH in the precursor solution or from the atmosphere during film formation leads to partial solvation of the methylammonium (MA⁺) "self-healing" of the perovskite lattice, resulting in significantly improved open-circuit voltage (V_{OC}) . [13] In a different study, it was found that additives such as MACl (methyl ammonium chloride) in combination with RH help the stabilization of the α -FAPbI₃ phase by enhancing the vaporization of residual MACl.^[12] The effect of RH on the fabrication of MHPs is a topic of ongoing debate and significantly depends on the precursor chemistry.[12-14]

In this work, we develop a machine learning (ML)-guided closed-loop platform named "AutoBot" to predict RH-dependent synthesis-property relationships for Cs_{0.1}FA_{0.9}PbI₃perovskite.This objective is accomplished through quantifying the combinatorial interplay between humidity during spin coating, (annealing temperature, annealing time, antisolvent drop time) while keeping the precursor chemistry constant. A core component of AutoBot is a multimodal characterization approach that integrates photoluminescence (PL) imaging, UV-vis, and PL spectroscopy to establish a film quality metric. Our active learning framework enables minimal experimental sampling where Bayesian optimization (BO) identifies the most informative experiments to construct synthesis-property relation maps. SHapley Additive exPlanations (SHAP) analysis enables rapid quantification of the feature

importance in our 4D parameter space and identifies the spin coater RH as the most important contribution to sample quality. The iterative learning loop was stopped when the subsequent information gain showed a rapid decrease in the learning rate to $\approx\!2\%$ after experimentally sampling less than 1% of the possible 5000+ combinations. Lastly, in situ photoluminescence characterization was used to investigate how RH regulates the MHP crystallization. High RH (>25–55%) enhances MACl vaporization, which likely led to the destabilization of the photoactive perovskite phase, consequently, poor film properties. Meanwhile, low RH (5–25%) promotes heterogeneous nucleation and α -perovskite phase stabilization. AutoBot accelerates the screening and understanding of the synthesis design space, facilitating rational synthesis recipe choice for a wide range of materials.

2. Results

The AutoBot closed-loop platform was designed to synthesize halide perovskite thin films (Cs_{0.1}FA_{0.9}PbI₃) from chemical precursor solutions with 10 mol% MACl additive to enhance crystallization control. ^[15] Thin film synthesis was followed by in-line optical characterization, namely UV–vis transmission, PL spectroscopy, and PL imaging (Figure 1; Figure S1a, Supporting Information). A typical loop of the automated platform consists of the following steps: a) chemical precursor solution deposition through spin coating, antisolvent treatment, thin film annealing, followed by coating with a protective Poly(methyl methacrylate) (PMMA) polymer layer. ^[16] b) in-line optical characterization; c) data extraction from spectra images, data fusion into a unitless total score (0–100) representing the film quality, where higher scores indicate higher quality; and d) ML suggestion of new experiments based on the *total score*.

Four synthesis parameters, the annealing temperature (100–200 °C, step size 10 °C), the annealing duration (5–60 min, step size 5 min), the antisolvent drop time (15-45 s, step size 5s), and the RH in the spin coater (5-55%, step size 10%) were varied. The RH in the spin coater was varied by purging dry or wet N₂ into the coater while depositing the film (see close-up photographs of the purging setup in Figure \$1b,c, Supporting Information). It is noted that AutoBot is operated in a fume hood where the RH during annealing was not controlled but recorded to be typically between 40-60%. The four synthesis parameters create a combinatorial parameter space with 5000+ possible combinations, and their optimal combination at different RH is unknown. Each set of synthesis conditions (referred to as a batch) is executed four times under nominally identical conditions, producing four samples per batch (see sample photographs, spectral imaging data in Figures S2-S5 and Table S1, Supporting Information).

2.1. Multimodal Data Fusion: Extracting the Total Score

A key challenge in automating synthesis decision-making based on multiple characterization techniques is obtaining machine-readable metrics that accurately represent material quality. While some studies have proposed extracting numerical metrics from single-characterization techniques (e.g., microscopy or

S. Arnold, Y.-R. Liu

Institute of Materials for Electronics and Energy Technology (i-MEET)
Department of Materials Science and Engineering
Friedrich-Alexander-Universität Erlangen-Nürnberg
91058 Erlangen, Germany

N. Thalanki
Department of Materials Science and Engineering
University of California
Berkeley, CA 94720, USA

16146840, 0, Downloaded from https://advanced.onlinelibrary.wiley.com/doi/10.1002/aenm.202502294 by University Of California - Davis, Wiley Online Library on [16.07/2025]. See the Terms and Conditions (https://advanced.onlinelibrary.wiley.com/doi/10.1002/aenm.202502294 by University Of California - Davis, Wiley Online Library on [16.07/2025]. See the Terms and Conditions (https://advanced.onlinelibrary.wiley.com/doi/10.1002/aenm.202502294 by University Of California - Davis, Wiley Online Library on [16.07/2025]. See the Terms and Conditions (https://advanced.onlinelibrary.wiley.com/doi/10.1002/aenm.202502294 by University Of California - Davis, Wiley Online Library on [16.07/2025]. See the Terms and Conditions (https://advanced.onlinelibrary.wiley.com/doi/10.1002/aenm.202502294 by University Of California - Davis, Wiley Online Library on [16.07/2025]. See the Terms and Conditions (https://advanced.onlinelibrary.wiley.com/doi/10.1002/aenm.202502294 by University Of California - Davis, Wiley Online Library on [16.07/2025]. See the Terms and Conditions (https://advanced.onlinelibrary.wiley.com/doi/10.1002/aenm.202502294 by University Of California - Davis, Wiley Online Library on [16.07/2025]. See the Terms and Conditions (https://advanced.onlinelibrary.wiley.com/doi/10.1002/aenm.202502294 by University Of California - Davis, Wiley Online Library on [16.07/2025]. See the Terms and Conditions (https://advanced.onlinelibrary.wiley.com/doi/10.1002/aenm.20250294 by University Of California - Davis, Wiley Online Library on [16.07/2025]. See the Terms and Conditions (https://advanced.onlinelibrary.wiley.com/doi/10.1002/aenm.20250294 by University Of California - Davis, Wiley Online Library on [16.07/2025]. See the Terms and Conditions (https://advanced.onlinelibrary.wiley.com/doi/10.1002/aenm.20250294 by University Of California - Davis, Wiley Online Library on [16.07/2025]. See the Terms and Conditions (https://advanced.onlinelibrary.wiley.com/doi/10.1002/aenm.20250294 by University Of California - Davis Of California

ditions) on Wiley Online Library for rules of use; OA articles are governed by the applicable Creative Commons

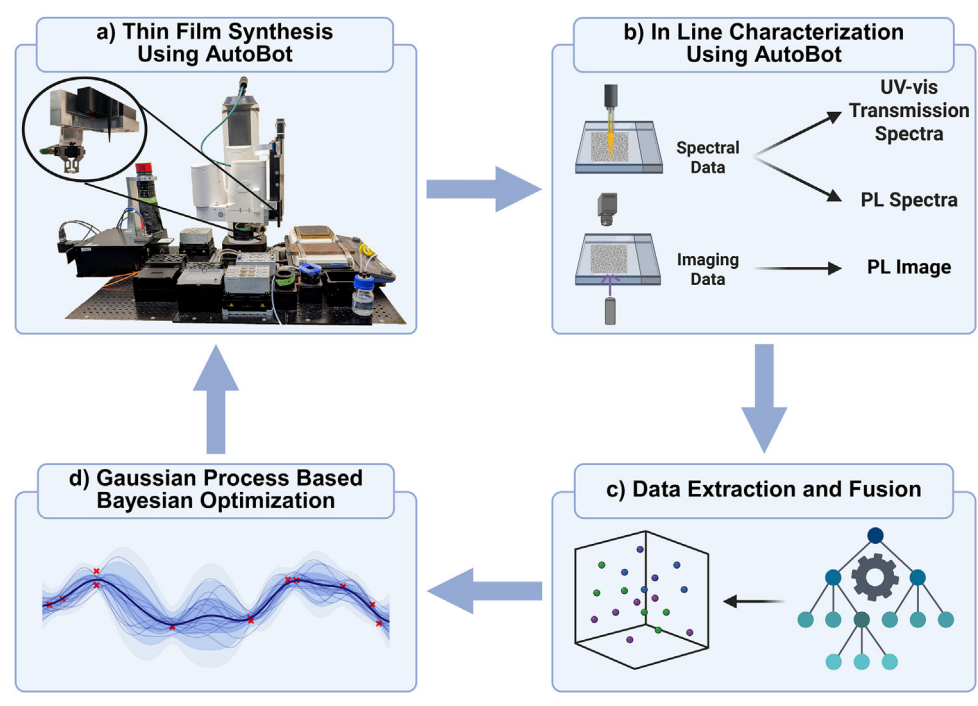


Figure 1. Schematic representation of the closed-loop platform. a) Photograph of the AutoBot synthesis and in-line characterization platform, b) schematic of in-line optical characterization, c) dimensional data reduction and fusion, d) ML input to define the next experiment.

spectroscopy), in practice, scientists typically rely on multiple characterization methods to comprehensively evaluate synthetic outcomes.^[17,18] In this work, a data fusion approach (Figure 2) was developed by combining spectroscopic datasets collected in two different modes with imaging data to provide a holistic evaluation of the perovskite film quality. First, UV–vis transmission spectra, PL spectra, and PL imaging data were collected. Second, we developed a metric to represent the film quality from each characterization. Third, metrics from the three characterizations

were weighted and combined into a single unitless *total score* that serves as a target for machine learning exploration. The weights for UV–vis spectra, PL spectra, and PL imaging were 40 – 20 – 40. Spectral PL was weighted lower because high levels of humidity lead to lower nucleation density, larger grains, thus high PL emission intensity, but poor substrate coverage (compared in Figure S6, Supporting Information; see Methods section for additional explanations). A high *total score* represents an optically dark, highly emissive, smooth and at the same time uniform,

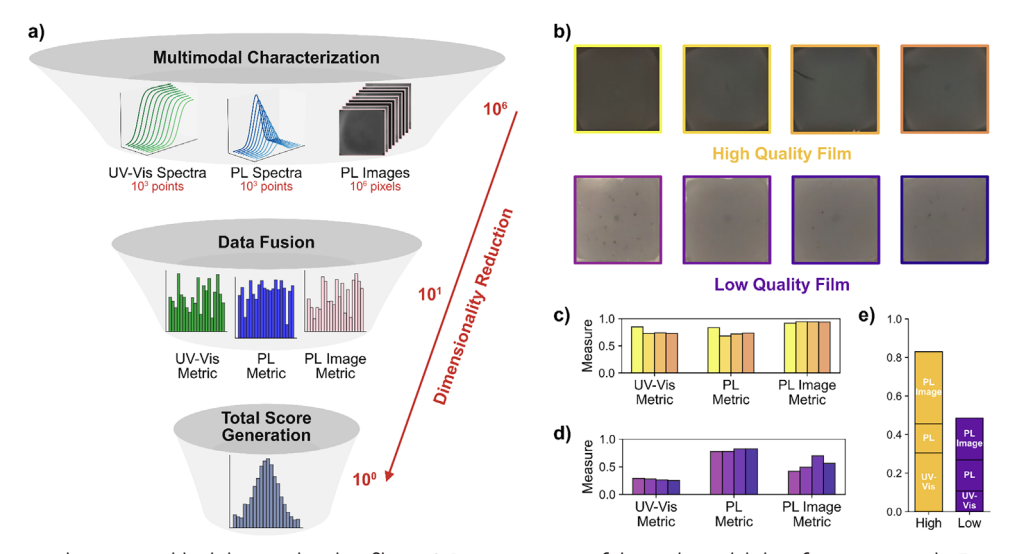


Figure 2. Data fusion schematic and high-low quality thin films. a) Representation of the multimodal data fusion approach. First input data (UV–vis transmission spectra, PL spectra, and PL images) is collected, followed by dimensional data reduction, and lastly data fusion into a *total score* through the weighted sum of individual components. b—e) Examples of high-low quality MHPs films (i.e., two batches with four nominally identical films), their individual metrics, *total score*.

16146840, 0, Downloaded from https://advanced.onlinelibrary.wiley.com/doi/10.1002/aenm.202502294 by University Of California

Davis, Wiley Online Library on [16/07/2025]. See the Terms and Conditions (https://onlinelibrary.wiley.com/term

-conditions) on Wiley Online Library for rules of use; OA articles are governed by the applicable Creative Commons

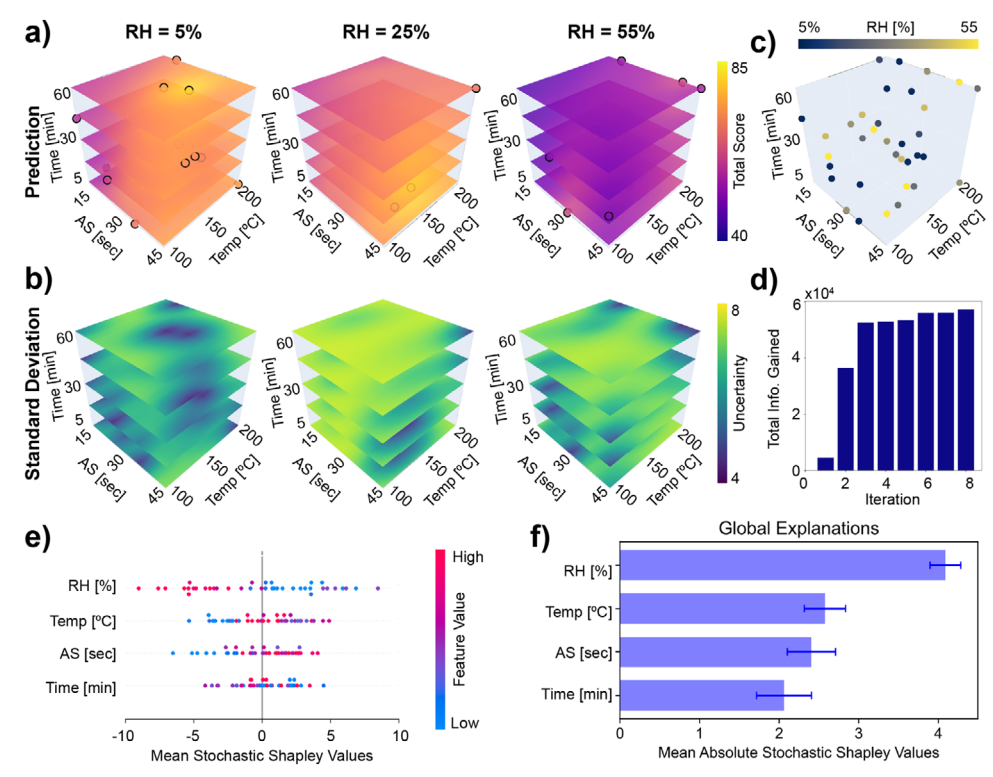


Figure 3. Machine learning and Bayesian optimization results. a) Gaussian process regression predicted synthesis—property relation maps illustrating the *total score* in relation to the annealing time (Time), antisolvent drop time (AS), and annealing temperature (Temp), binned at different RH. Black circles represent individual experimental points. b) Corresponding uncertainties to (a), binned at different RH. c) 4D parameter space representing the 40 experimental batches fabricated. d) Cumulative total information gain (or cumulative Kullback-Leibler divergence). e,f) Global feature importance ranking obtained from SHAP analysis showing the importance of synthesis conditions in descending order of importance (rank). The standard deviations are attached to each mean value.

fully covering MHP thin film, while a low score represents a poor quality inhomogeneous thin film, which aligns with the domain experts' manual evaluation (Figure 2b–e). See methods and SI for more details (Figures S7–S11, Table S1, Supporting Information, last four columns). It is noted that the overarching goal of our study was the development of a generalizable workflow for a materials acceleration platform. A crucial step in any materials optimization, including device fabrication, is the definition of processing windows.^[19] In this respect, our approach could be modified in future experiments and also used in the next stage to explore device-related aspects.

2.2. Active Learning-Assisted Generation of Synthesis-Property Relation Maps

Next, ML was applied to efficiently explore the parameter space with 5000+ possible experimental combinations. Bayesian optimization (BO) algorithms have been used in the MHP field to optimize material quality reproducibility as well as stability. [11,20] Here, we used Gaussian process regression (GPR) to predict synthesis—property relation maps of the *total score*, considered as a proxy for the quality of the MHP film, to the process parameters $\mathbf{x} = \{x_1, x_2, x_3, x_4\} \subset \mathbf{X}$ where x_1 to x_4 are the antisolvent drop time, annealing temperature, annealing time, and spin-coater relative humidity, respectively. Specifically, GPR was chosen be-

cause of its ability to stochastically approximate unknown functions using small datasets compared to other ML models.[21-23] Furthermore, a key advantage of the GPR lies in its inherent ability to estimate the uncertainty associated with its predictions, which is crucial when identifying new experiments during iterative closed-loop active learning efforts. To leverage this capability, a BO approach with the total correlation acquisition function was implemented to explore the parameter space efficiently.^[24] The total correlation acquisition function identifies points that are least correlated with each other and with the previously tested points to maximize the information gained from each experiment. Herein, our analysis started with 16 randomly selected points in the parameter space in iteration zero. During each subsequent iteration, the BO uses previous experiments to identify three future conditions to test. More details about GPR BO are provided in the Methods section.

The GPR model predicted synthesis-property relations across varying spin coater RH levels (5–55%) and provided their uncertainties (**Figure 3a**,b; Figure **S12**, Supporting Information) represented by the standard deviation of the *total score* distribution. The highest *total scores* (>80) were found and predicted for experiments conducted in a RH window between 5–25% (Figures **S11** and **S12**, Supporting Information). At RH \geq 35%, the best predicted *total scores* are \leq 66. Therefore, there seems to be a processing window between 5–25% RH where similar quality halide perovskite films can be obtained by adjusting the annealing

ADVANCED ENERGY MATERIALS 16146840, 0, Downloaded from https://advanced.onlinelibray.wiley.com/doi/10.1002aenn...0292294 by University Of California - Davis, Wiley Online Library on [1607/2025]. See the Terms and Conditions (https://onlinelibrary.wiley.com/terms-and-conditions) on Wiley Online Library for rules of use; OA articles are governed by the applicable Creative Commons Licenses

temperature to an average of 170 °C, the antisolvent drop time after 35–40 s, and the annealing time to a maximum of 25 min. One well-discussed reason for this relatively higher annealing temperature, when compared to the prototype MAPbI $_3$ (MA = methylammonium) perovskite, is the competition between the non-photoactive $\delta_{\rm H}$ - and photoactive α -FAPbI $_3$ phases. [25] The transition from $\delta_{\rm H}$ - α -FAPbI $_3$ was found at 165 °C, while alloying with Cs leads to a decrease in the transition temperature with increasing Cs ratio. [25] This also explains why the *total score* is typically lower for samples annealed at temperatures \leq 130 °C. The suitable temperature range is consistent with previous studies on FAPbI $_3$ and CsFAPbI $_3$. [26–28]

The iterative process stopped after eight BO iterations (40 batches corresponding to 160 samples, see Figure 3c), sampling less than 1% of the total parameter space. A stopping criterion based on information gained from experiments was used to identify when information gain became limited (≈2% over five consecutive iterations) through additional experiments. This implied that continuing experiments would not significantly improve the predictions. Specifically, the Kullback-Leibler (KL) divergence was used to compute the difference between the GP model before and after adding the new experiments. A large KL value indicates that the new experiments significantly changed the GP model predictions, resulting in improved synthesis-property relation predictions. The steep initial increase in the total KL in Figure 3d indicates that the early experiments yielded substantial information gain about this relation.

To better understand how different synthetic factors contribute to the overall total score, we performed a SHapley Additive ex-Planations (SHAP) analysis on the GPR model to evaluate the relative contributions from each synthetic factor to the films' total score (more details are provided in the Methods section). [29,30] The SHAP summary plot in Figure 3e, where red points indicate high feature values, blue points represent low values, confirms that RH during spin coating is the most influential factor, while annealing time has the smallest impact; annealing temperature and antisolvent drop time exhibit intermediate contributions. Figure 3f further highlights that all four synthesis parameters have measurable importance in the model's output, demonstrating that, despite RH having the highest influence, the remaining parameters still play non-negligible roles. To evaluate feature interdependence, we added a Pearson correlation heatmap (Figure S13, Supporting Information) in addition to the SHAP analysis, which shows low off-diagonal coefficients among the four synthesis parameters. Together, Figure 3e,f and Figure \$13 (Supporting Information) demonstrate that while RH is the dominant factor, the other synthesis parameters independently and meaningfully contribute to the film quality. Based on these insights, next, we used the GPR prediction to select experimental conditions for more detailed manual in situ PL characterizations.

2.3. Manual in Situ PL Characterization to Gain Mechanistic Insights and Explain the *Total Score*

The SHAP analysis identified the RH during spin coating as the most important feature contributing to the *total score*. As a next step, we identify experimental conditions based on the GPR predictions by illustrating the best (99th percentile) and worst (1st

percentile) synthesis–property relationship windows (**Figure 4a**). Then, we manually collect in situ PL measurements (see Methods section for a description of the setup). Since the antisolvent dropping during spin coating triggers nucleation and growth, [31] we investigate the correlation between nucleation and growth dynamics in different RHs, choosing the ideal antisolvent drop times at 5, 25, and 55% RH (Figure 4b–d). The antisolvent drop times predicted by the GPR were 35, 40, and 40s of the total spin coating time for 5, 25, and 55% RH, respectively. These drop times correlate well with literature reports. [32,33]

The PL signals appear immediately when dropping the antisolvent (illustrated by the vertical narrow window, Figure 4b), indicating perovskite nucleation.[34,33] From low to high RH, the final PL emission position was observed at 1.63, 1.62, and 1.58 eV, respectively (Figure 4c). Clearly, the higher the RH during spin coating, the larger the magnitude of the red shift, defined as the difference between the initial/final center peak positions. It increases from 27 to 50 meV, and 61 meV at 5%, 25%, and 55% RH, respectively. Furthermore, the PL intensity constantly drops from low to high RH. The final peak position of 1.54 eV is not reached during spin coating, because the film requires subsequent annealing to evaporate the MACl additive and the residual Lewis base molecules in the intermediate phases.^[15] This indicates a correlation between RH, MACl additive, and the nucleation/growth mechanism. The strong interaction between hygroscopic MACl and the water molecules can lead to a destabilization of MA-rich α-phase nuclei related to enhanced MACl evaporation at higher RH.[12] This can also be seen in the magnitude of the PL shift, which is the largest at the highest RH because of less MA incorporation. At high RH, α-FAPbI₃ nuclei become less stable at room temperature because the lattice constant is too small to form α -phase. Instead, the thermodynamically more stable delta phase will form.[25] Lastly, Figure 4d summarizes the integrated PL spectra during the antisolvent dropping with a single Gaussian fit to the data. The fit quality is the best at high RH and the PL peak FWHM is the narrowest, likely because of better nuclei uniformity and more homogeneous nucleation. In contrast, a broad emission peak is observed at both 5% and 25% RH. At these lower RHs, more MACl is present to facilitate nuclei with a wider compositional variation where the MA+ cation from the MACl additive initially participates in forming an intermediate phase (e.g., MA, Cs, FA, Pb(I,Cl)₃), as well as heterogeneous nucleation. Both can explain the broader FWHM. Heterogeneous nucleation is desirable to facilitate perovskite growth with preferential orientation, enhanced crystallinity, reduced defect formation, and grain boundaries to result in pin-hole free, high-quality MHP films.^[35] It has been reported before that MA⁺ from MACl is incorporated in the perovskite intermediate phase at room temperature.^[15] Scanning electron microscopy (SEM) images taken at different RH levels illustrate poor substrate coverage if films are made under high RH, while uniform films (with full coverage) are observed at 5, 15, 25% RH (Figure \$14, Supporting Information). By adjusting the antisolvent drop time, similar MHP film quality can be obtained in a relative humidity window between 5%-25%, as confirmed by X-ray diffraction (XRD), time-resolved PL (TRPL), and SEM measurements (see Figure \$14, Supporting Information). The lifetimes at low to moderate RH are comparable to literature values for Cs_{0.1}FA_{0.9}PbI₃.^[36,37] The highest lifetime was observed for the sample made at 55% RH, which is explained

onlinelibrary.wiley.com/doi/10.1002/aenm.202502294 by University Of California - Davis, Wiley Online Library on [16/07/2025]. See the Terms and Conditions (http://original.com/doi/10.1002/aenm.202502294 by University Of California - Davis, Wiley Online Library on [16/07/2025]. See the Terms and Conditions (http://original.com/doi/10.1002/aenm.202502294 by University Of California - Davis, Wiley Online Library on [16/07/2025]. See the Terms and Conditions (http://original.com/doi/10.1002/aenm.202502294 by University Of California - Davis, Wiley Online Library on [16/07/2025]. See the Terms and Conditions (http://original.com/doi/10.1002/aenm.202502294 by University Of California - Davis, Wiley Online Library on [16/07/2025]. See the Terms and Conditions (http://original.com/doi/10.1002/aenm.202502294 by University Of California - Davis, Wiley Online Library on [16/07/2025]. See the Terms and Conditions (http://original.com/doi/10.1002/aenm.202502294 by University Of California - Davis, Wiley Online Library on [16/07/2025]. See the Terms and Conditions (http://original.com/doi/10.1002/aenm.202502294 by University Of California - Davis, Wiley Online Library on [16/07/2025].

nditions) on Wiley Online Library for rules of use; OA articles are governed by the applicable Creative Commons License

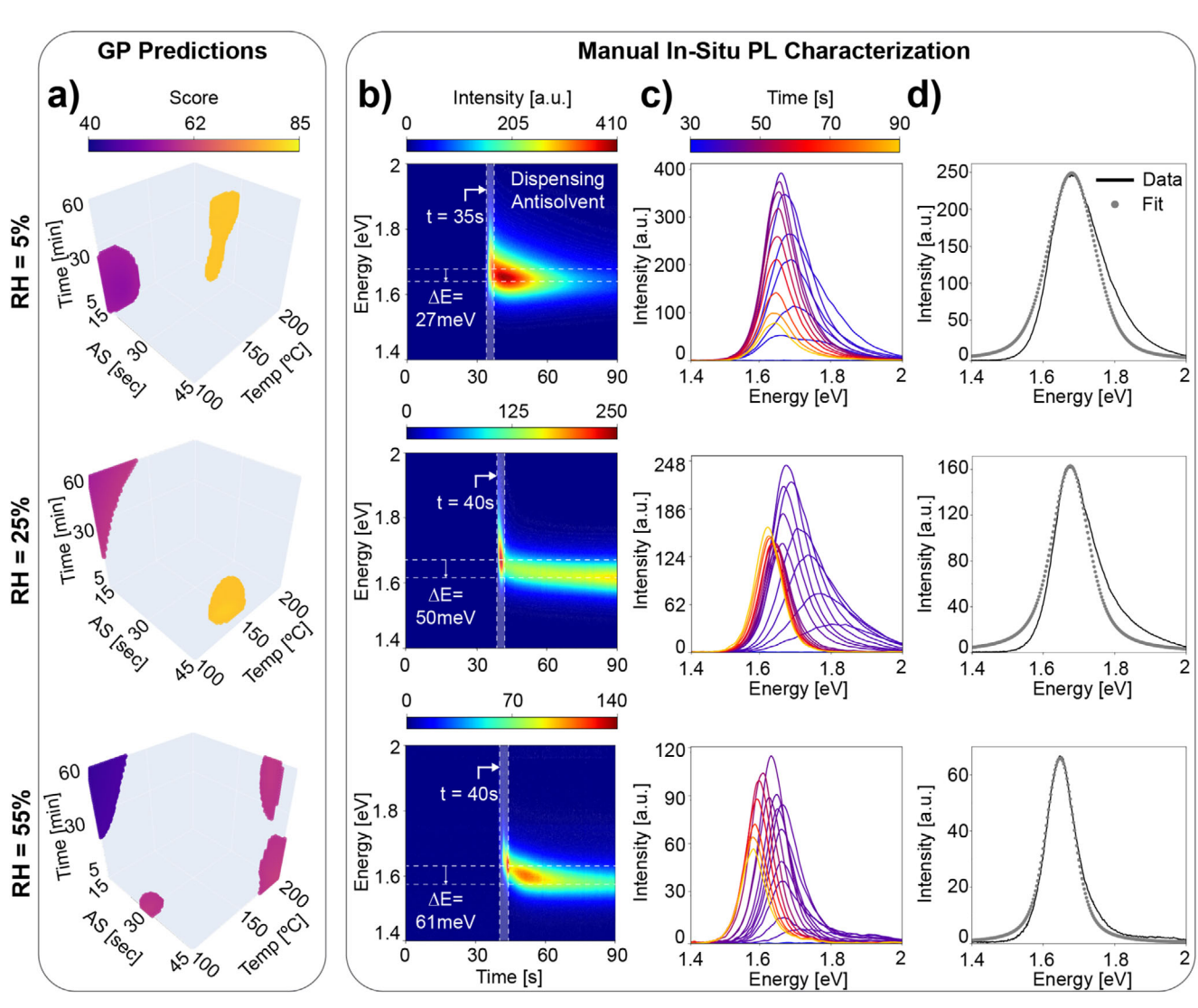


Figure 4. Using GPR predictions to inform selected manually performed in situ PL measurements at increasing RH levels (top to bottom: 5, 25, and 55% RH). a) Predicted synthesis—property relationship windows for the top and bottom 1%. b) Contour plots representing the evolution of PL spectra over time collected during the spin coating and antisolvent dropping. The vertical line illustrates the antisolvent drop time. c) Individual PL spectra taken at different times during the spin coating. d) Averaged PL spectra appearing during the antisolvent dropping with a single Gaussian fit.

by the large μ m-sized grains obtained from a lower nucleation density and correlates with literature reports. [13] In summary, decreasing the energetic barrier to form heterogeneously nucleating α -FAPbI $_3$ can be achieved through fine-tuning of the RH for Cs $_{0.1}$ FA $_{0.9}$ PbI $_3$ with 10 mol% MACl additive. To explore this further, the interplay between RH and MACl additives presents a successful avenue to control the Cs $_x$ FA $_{1-x}$ PbI $_3$ crystallization.

3. Conclusion

Through the implementation of the closed-loop AutoBot platform, we demonstrated the synergy between automated thin film synthesis characterization, dimensional data reduction and fusion, and AI-guided parameter space exploration. ML was used to predict synthesis–property relation maps, which connect the fabrication parameters (annealing temperature, annealing time, antisolvent drop time, and spin coater RH ranging from 5% to

55%) to the predicted film total score. The total score was constructed through data fusion of spectral and imaging data, and the maximum uncertainty of the predicted synthesis-property relation maps is about one standard deviation. After experimentally sampling less than 1% of the possible 5000+ combinations, the learning rate dropped significantly to ≈2%, confirming the effectiveness of the closed-loop exploration approach. Feature importance ranking through SHAP analysis revealed the RH during spin coating as a major contribution to the total score. In the last step, we validated the predicted synthesis-property relations through manual in situ photoluminescence characterization during the spin coating step at different RHs. Our data imply that higher RH aids methylammonium chloride additive vaporization, as evidenced by the final PL peak position and total peak position shift. Simultaneously, it leads to less stable nuclei because of the interplay of photoactive α - and non-photoactive δ_{H} phases as seen in the overall lower PL intensity. We reveal that the

ADVANCED ENERGY MATERIALS 16146840, 0, Downloaded from https://advanced.onlinelibrary.wiley.com/doi/10.1002/aems.202592594 by University Of California - Davis, Wiley Online Library on [1607/2025]. See the Terms and Conditions (https://onlinelibrary.wiley.com/erms

and-conditions) on Wiley Online Library for rules of use; OA articles are governed by the applicable Creative Commons

RH decreases the energetic barrier to form heterogeneously nucleating $\alpha\text{-}\text{FAPbI}_3$ in the presence of MACl. This demonstrates a successful avenue for controlling the $\text{Cs}_{0.1}\text{FA}_{0.9}\text{PbI}_3$ crystallization. By adjusting the antisolvent drop time, similar MHP film quality can be obtained in a relative humidity window between 5%–25%, lifting the need for stringent atmospheric control. Our AutoBot MAP accelerates the screening of the synthesis design space, reducing the time cost needed to define global maxima in the synthesis parameter window. This presents a significant step toward establishing autonomous laboratories for the optimization of synthesis parameters. We envision this closed-loop approach to be of use for a wide range of materials, including polymers sol-gel synthesized oxide materials synthesis optimization efforts.

4. Experimental Section

Materials: Cesium iodide (CsI, 99.999%), anhydrous N, N-dimethylformamide (DMF, 99.8%), dimethyl sulfoxide (DMSO, 99.9%), and chlorobenzene (CB, anhydrous, 99.8%) were purchased from Sigma–Aldrich. Lead(II) iodide (PbI2, 99.99%) was purchased from Tokyo Chemical Industry (TCI). Formamidinium iodide (FAI, 99.99%) and methylammonium chloride (99.99%) were purchased from Great-cell Solar Ltd. All reagents were employed as received without further purification or additional treatment.

Thin Film Precursor Preparation (Stock Solutions): Thin films were prepared with 1.6 M precursors based on $Cs_{0.1}FA_{0.9}PbI_3$ by dissolving 26 mg CsI, 154.8 mg FAI, 461 mg PbI $_2$, 6.8 mg MACl in 0.500 ml DMF, 0.125 ml DMSO, and stirring for 2–3 h. Stock solutions were prepared in a N_2 glovebox, stored in a N_2 glovebox, and used for up to one week. The $Cs_{0.1}FA_{0.9}PbI_3$ perovskite composition was chosen because of its better relative stability compared to FAPbI $_3$. Different MACl additive contents ranging from 5 to 40 mol% were used in previous reports, varying depending on the precursor chemistry as well as deposition atmosphere. Based on these numbers and preliminary stability tests, 10 mol% MACl was selected.

Poly(methyl methacrylate) (PMMA) polymer dispersion was made by dissolving 10 mg of PMMA in 1 mL Chlorobenzene.

Substrate Cleaning: $15 \times 15 \text{ mm}^2$ glass substrates were sonicated in soap water, DI water, acetone, IPA solvent for 10–15 min each. The substrates were then dried with N $_2$ and treated with UV-Ozone for 60 min before use.

Thin Film Preparation: Spin coating was performed at 1,000 rpm for 10 s, followed by 5000 rpm for 15-45 s. The antisolvent chlorobenzene was dropped at 15-45 s of the total spin coating duration and 10 s before the spin coating ended. The total spin coating time was 25-55 s, depending on the antisolvent drop time. The boundaries step sizes for the four synthesis parameters were set as follows: annealing temperature (100–200 $^{\circ}$ C, step size of 10 °C), annealing duration (5-60 min, step size 5 min), antisolvent drop time (15-45 s, step size 5s), and RH during spin coating (5%, 15%, 25%, 35%, 45%, 55%, step size 10%). The RH in the spin-coater was controlled between ≈5–55% via purging dry or wet N₂ into the spincoater during deposition. The wet N2 gas was obtained through bubbling N2 through water. The humidity in the spin-coater was monitored using an AHT20 humidity sensor. The RH during spin coating was adjusted with 5% precision (i.e., 0-5%, 10-15%, 20-25%, 30-35%, 40-45%, 50-55%) was referred to by the upper limit at each step, e.g. 0-5% is mentioned as 5% RH so on. We note that the RH upper bound was set to 55%. However, the overarching goal of our study is to develop a generalizable workflow to predict the outcome (total score) for the four synthesis parameters. Although we choose annealing temperature, annealing duration, antisolvent drop time, and spin coater RH, as well as their boundary step sizes, the framework could be modified and other parameters as well as different boundaries can be used as relevant to the material system and particular laboratory setting. In this study, we limited the spincoater humidity to the average indoor humidity in the USA, which generally stays below 60%. Thin film annealing was performed in the fume hood, where RH is recorded but not controlled. For the batches reported here, the fume hood RH was between 40-60% (measured far away from the hot plate). Since RH is temperature dependent, it was also measured in close proximity to the sample on the hot plate (see Table S4, Supporting Information). After sample annealing, the films are coated with a Poly(methyl methacrylate) (PMMA) polymer protection layer within 5 min to enhance the stability of the perovskite film, ensuring reliable data during characterization. [16] It is noted that all the thin film synthesis characterization was performed in an ambient atmosphere at an oxygen content of \approx 21% by volume. In a prior study it was found for MAPbI₃ that oxygen might be linked to the formation of PbI₂. [40] The diffraction patterns in Figure S14 (Supporting Information) do not show any evidence of PbI2. Additional studies will be needed to draw clear conclusions.

Thin Film Characterization: Home-built optics were used for the inline optical characterizations described here. UV–vis transmission spectra were collected using a Thorlabs Quartz-Tungsten-Halogen (QTH 10) white light source. The transmitted signal was collected with a fiber-coupled Flame spectrometer with CCD detector array (FLAME-S-VIS-NIR-ES, FLMS12833). A line scan measurement consisting of eight spots was performed off-center.

Spectral PL measurements in transmission mode were acquired using a 530 nm fiber-coupled LED (M530F2) and a 550 nm shortpass filter. The emission signal was collected after a 600 nm longpass filter with a fiber-coupled Flame spectrometer with CCD detector array. PL imaging data was conducted in a transmission geometry. A 405 nm LED (Thorlabs M405L4) served as the excitation light source. The LED light was collimated using a 25 mm plano-convex N-BK7 lens (Thorlabs) diffused by a patterned square diffuser (Thorlabs ED1-S20-MD) to match the shape of the deposition substrates. The excitation light was filtered using a 450 nm short-pass optical filter (Thorlabs FESH0450), while the emission was isolated with a 550 nm long-pass optical filter (Thorlabs FELH0550).

PL images were captured using a high-resolution CMOS camera (ZWO ASI294MC) equipped with a 2x macro lens (Laowa Ultra-Macro APO). Each image had a resolution of 4144×2822 pixels, with a nominal pixel size of 6 μ m. Exposure times were automatically adjusted for each sample but typically ranged between 2–8 μ s.

Each sample is characterized spectroscopically by line scans taking eight UV–vis transmission and PL spectra across a sample (Figures S3 and S4, Supporting Information) through a PL image (Figure S5, Supporting Information), respectively. Figure S10 (Supporting Information) summarizes the means and standard deviations of these eight measurements for all samples across all batches for UV–vis (a) and PL spectra (b). Given that the standard deviation of most of the samples is relatively low, in the subsequent analysis, we only consider the mean values per sample. Synthesis characterization of a batch that took between 30–90 min is dominated by the annealing duration.

Data Processing & Dimensionality Reduction: To analyze the UV-vis spectra, we defined a transmission ratio to perform a computational analysis designed to characterize spectral deviations from ideal behavior. First, the Tauc plot analysis was performed to determine the optical bandgap of the sample by converting the measured transmission spectrum into the absorption coefficient, $\alpha(\lambda)$. The collected spectral data were first corrected by accounting for dark current reference intensity, followed by applying Gaussian smoothing to reduce noise. The absorption coefficient was then computed using the Beer-Lambert law, where the optical thickness was assumed to be roughly constant at 700 nm based on scanning electron microscopy cross-section images. The photon energy (hv) was calculated from the wavelength using the relation $h\nu = 1240/\lambda$, and the Tauc exponent (n = 2) was chosen for a direct bandgap material. A linear fit was applied to the Tauc plot within a selected energy range (1.54-1.58 eV) to determine the bandgap energy by extrapolating to the x-axis. The estimated bandgaps, as shown in Figure S7 (Supporting Information) (between 1.44-1.53 eV), were then averaged, resulting in a mean bandgap of 1.50 eV, corresponding to a wavelength of 826 nm. Considering that there are differences in the syntheses, such as through additives

16146840, 0, Downloaded from https://advanced.onlinelibrary.wiley.com/doi/10.1002/aenm.202502294 by University Of California - Davis, Wiley Online Library on [16.07/2025]. See the Terms and Conditions (https://onlinelibrary.wiley.com/terms-

-and-conditions) on Wiley Online Library for rules of use; OA articles are governed by the applicable Creative Commons

or the synthesis environment, which might affect the bandgap, this number is in agreement with the literature on $Cs_{0.1}FA_{0.9}PbI_3$. [41,42] This absorption feature was used to divide the transmission spectra into four areas, using the trapezoidal rule, as shown in Figure S8 (Supporting Information), followed by a computational analysis procedure designed to characterize spectral deviations from ideal behavior. The ideal behavior was assumed to be a step function, with 0% 100% transmission at wavelengths below and above the bandgap, respectively. High transmittance above the bandgap wavelength was previously linked to low light scattering and, therefore, uniform smooth film morphology. [43] The metric from UVvis transmission spectra is the ratio of area 1/area 2 (Figures S7 and S8, Supporting Information), with higher ratios reflecting thicker films, better substrate coverage, and higher content of the α -FAPbI₃ phase rather than δ_{H} -FAPbl₃. Although the theoretical limit approaches infinity, that is not possible experimentally, as some degree of scattering will be observed. Experimentally obtained UV Vis ratios ranged from 1-5. The standard deviation of the UV-vis metric per batch is listed in Table S2 (Supporting Information).

Photoluminescence (PL) intensity analysis was performed using spectral PL data, which was corrected for dark counts and reference light source spectrum before applying a Jacobian transformation to convert wavelength-dependent intensity into energy-dependent intensity. The Jacobian transformation was applied using the relation $J(E) = 1240/E^2$ to ensure a proper representation of PL spectra in the energy domain. [44] The transformed PL spectrum was then fitted using a combination of a linear background a Pseudo-Voigt peak function, which accounts for both Gaussian and Lorentzian broadening effects. This peak function is frequently used for the evaluation of PL spectra, as for example described in the SI^[45] or for the analysis of multiband PL spectra. [46] The peak integration was performed using numerical integration (trapezoidal method) over the fitted peak component, providing an area-under-the-curve (AUC) value that quantifies the total emitted PL intensity. Figure S6 (Supporting Information) illustrates a significant difference in PL intensity for samples made in extremely different RH, but little variation in FWHM. Consequently, the AUC was chosen as the PL metric. The standard deviation of the PL metric per batch is listed in Table S3 (Supporting Information).

The PL imaging heterogeneity metric was derived from PL images, which were first preprocessed to remove extraneous elements such as the sample holder, followed by normalization to standardize image intensity and minimize variations due to lighting conditions. After preprocessing, three quantitative features were extracted to characterize spatial structural variations in PL emission, as shown in Figure S9 (Supporting Information). The first feature, standard deviation, quantified spatial fluctuations in PL intensity across the sample, capturing variations in emission uniformity. The second feature, entropy, was computed from the normalized histogram of pixel intensities, providing a measure of disorder and defectinduced variations under different humidity conditions. The third feature, radial intensity standard deviation, was determined by segmenting the image into concentric rings of 50-pixel width, computing the average intensity within each ring, and identifying local extrema in the resulting intensity profile. A higher number of extrema indicated non-uniformity in the PL response, which is associated with defects. To quantify this, the intensity profile was divided into sub-intervals, and the variance within each interval was computed. Since a greater number of extrema suggested higher defect density, a penalty was applied using the equation

Radial Intensity Standard Deviation =
$$N\sqrt{\sum_{i}^{N} Var(i)}$$
 (1)

where N represents the number of sub-intervals, Var(i) represents the variance of each interval. This approach effectively penalized samples with greater structural inhomogeneity, ensuring that more defective samples received a higher heterogeneity metric. Spin coating is a radial coating process where the robot applies the liquid coating solution to the center of the substrate, which is then spun at high speed. The centripetal force causes the liquid to spread radially outward across the substrate surface. This coating process can result in radial (unwanted) features, e.g., if

the antisolvent timing is not perfect (see sample photos in S2). Consequently, this is an important metric to take into account when evaluating film homogeneity. Finally, the three features were combined into a single heterogeneity metric using a weighted summation, with standard deviation, entropy, and radial intensity standard deviation assigned weights of 20%, 10%, and 70%, respectively. This integrated approach enabled a systematic comparative evaluation of perovskite heterogeneity across different synthesis conditions and humidity environments, providing a robust framework for assessing film stability. The PL imaging heterogeneity metric is supposed to be as small as possible for homogeneous samples taken as the additive inverse (i.e., 1 – PL imaging metric).

Total Score: To calculate the total score, each of the three features was given a weight based on its significance compared to ground truth samples made by a human expert in a N2-filled glovebox. With the goal of achieving optically dark, smooth, high-quality, uniform, fully covering halide perovskite thin film samples, the weights of 40-20-40 for UV-vis spectral PL - PL imaging, respectively, were assigned. UV-vis and PL imaging was each given a higher weight (40%) due to their direct correlation with film morphology uniformity, respectively. Spectral PL measurements were weighted at 20% because, on one hand, high PL emission intensity reflects high material quality; however, PL intensity is also influenced by morphological features. Homogeneous and fully covering polycrystalline thin films are desirable, but result in lower PL emission intensity than microcrystals withhigher PL emission intensity while only sparsely covering the substrate (see Figure S6, Supporting Information). Lastly, the standard deviation of PL spectral data compared to UV-vis data (Tables S2 and S3, Supporting Information) is larger. All these considerations led to the decision of choosing the weights of 40-20-40 for UV-vis - spectral PL - PL imaging

Manual In Situ Photoluminescence Measurements: In situ PL measurements were performed during spin-coating under controlled relative humidity (RH) conditions. A home-built optical setup consisting of a 405 nm laser diode, a plano-convex lens, a 450 nm long-pass filter, and a fiber-coupled Ocean Optics spectrometer (QE pro) calibrated by the manufacturer was used. The optical setup was placed over the spin coater to characterize the spin coating step. The RH in the spin coater volume was controlled by bubbling N_2 through water, adjusting the gas flow rate. Spectra were recorded every 100 ms during the measurement. PL emission spectra were fitted using Pseudo-Voigt peak fitting after the Jacobian transformation to the energy scale. To illustrate the averaged spectra when dropping the antisolvent, we integrated 30 spectra in the time frame of 3 s. Fitting was done with Voigt peak fitting for a single peak.

Machine Learning: Machine learning optimization techniques could be used to model the complex relationship between the process parameters and the film properties. Specifically, Bayesian optimization with a tailored acquisition function was implemented to explore and predict the film properties efficiently for any combination of the process parameters.

Gaussian Stochastic Process: GPR modeling was used to create synthesis-property maps relating the total score of the film to the process parameters. Among other ML techniques, GPR was chosen for its distinctive capabilities. Using relatively small datasets, it could efficiently stochastically approximate complicated (unknown) latent functions relating film synthesis parameters to quantifiable film properties. Its stochastic nature allows it to inherently quantify uncertainty, differentiating between aleatoric uncertainty, linked to inherent experimental results variability, and epistemic uncertainty, linked to the lack of enough data for accurate predictions. The uncertainty quantification capability of the GPR is essential for informed decision-making during parameter space exploration. This uncertainty quantifies the GPR model's confidence in its predictions, where lower uncertainty indicates higher confidence, while higher uncertainty suggests less reliable predictions. Moreover, unlike other machine learning models, the GPR model provides explicit, interpretable insights into the properties of the latent function. Additionally, GPR modeling does not require explicit specification of the functional form of the latent function, which becomes challenging to identify with high-dimensional param-

GPR modeling was used to predict the films' total score as a function of the process parameters $\mathbf{x} = \{x_1, x_2, x_3, x_4\} \in \mathbf{X} \subset \mathbb{R}^4$. Here, the consid-

ered parameter space is a 4D Euclidean bounded domain composed of the antisolvent drop time (x_1) , annealing temperature (x_2) , annealing time (x_3) , and spin-coater relative humidity (x_{44}) . The total score was considered an unknown latent function f(x) that could only be sampled using noisy measurements $y(\mathbf{x}) = f(\mathbf{x}) + \varepsilon(\mathbf{x})$, with $\varepsilon(\mathbf{x})$ being an independently identically distributed zero-mean noise. In this study, y (x) corresponds to the experimentally measured total score for each sample. To better quantify measurement variability, four samples were tested under each experimental condition x, referred to here as a batch, and these observations were incorporated into the GPR model. With this definition, the GPR provides a stochastic representation of the total score by characterizing a probability distribution for f(x). This was accomplished by assigning a prior multivariate normal probability distribution $\mathcal{N}(E[f(\mathbf{x}_i)], Cov[f(\mathbf{x}_i), f(\mathbf{x}_i)]) \ \forall \ i, j \in I$ $\{1, 2, ..., n\}$ with n being the number of tested data points to the latent function. This prior normal distribution is characterized by a prior mean vector $E[f(\mathbf{x}_i)] = \mu(\mathbf{x}_i; \boldsymbol{\Theta})$ and a covariance matrix $Cov[f(\mathbf{x}_i), f(\mathbf{x}_i)] = K =$ $k(\mathbf{x}_i, \mathbf{x}_i; \boldsymbol{\Theta})$, where μ is a prior mean function and k is a positive semidefinite kernel function acting on all pairs $\{x_i, x_i\}$. Both functions depend on hyperparameters that are included in Θ . The prior mean function encodes the expected general trend of the latent function over the parameter space prior to data collection. The film quality was expected to vary in the parameter space, but with an unknown trend. To incorporate this information while not biasing the predictions, the prior mean was chosen as a linear function of the four process parameters with slopes and an intercept to be learned from the data. On the other hand, the kernel function, the main component of a GPR model, acts as the covariance operator. It estimates the covariance between two latent function values $f(x_i)$ and $f(x_i)$ based on the data points x_i and x_i , even if they were not tested yet. Moreover, the kernel function estimates the uncertainty linked to the lack of enough data for accurate predictions — the so-called epistemic uncertainty — which is a key component in active learning efforts aiming toward efficient parameter space exploration. One of the most used kernel functions is the stationary v = 3/2 Matérn kernel that computes the covariance based on the Euclidean distance between x_i and x_i . Since the parameter space is composed of four parameters with different ranges and possibly different decay rates in the covariance, an anisotropic kernel function was used, with each parameter having its length scale determined by automatic relevance determination. Following the principles of Bayesian inference using the prior normal distribution $p(f|\Theta) = \mathcal{N}(\mu(x), k(x_i, x_i))$, GPR predicts the posterior distribution of the latent function $p(f^*|y, \Theta)$, where $f^* = f(x_i^*)$ are the predictions at unobserved points in the parameter space x_i^* , by incorporating a likelihood model defined over noisy data $\mathbf{y} = \mathbf{y}(\mathbf{x}_i) \ \forall \ i' \in \{1, 2, ..., n\}.$ This likelihood characterizes the probability of observing y given f, modeled as $p(\mathbf{y}|\mathbf{f}, \mathbf{\Theta}) = \mathcal{N}(\mathbf{f}, \mathbf{V}(\mathbf{\Theta}))$, where $\mathbf{V}_{ii} = \sigma_n^2(\mathbf{x}_i; \mathbf{\Theta})$ is a diagonal noise matrix with entries calculated using the noise function $\sigma_n^2(\mathbf{x}_i)$ that also depends on hyperparameters Θ . The noise function is used to quantify the aleatoric uncertainty that stems from the data variability. In this work, it is assumed that the variability of the total score is constant throughout the parameter space. To combine the above into a mathematical formulation, the GPR model is written as

$$y(\mathbf{x}) = f(\mathbf{x}) + \epsilon(\mathbf{x}) \tag{2}$$

$$f(\mathbf{x}) \sim GP(\mu(\mathbf{x}), k(\mathbf{x}_i, \mathbf{x}_j))$$
 (3)

$$\mu(\mathbf{x}) = c_1 x_1 + c_2 x_2 + c_3 x_3 + c_4 x_4 + c_5 \tag{4}$$

$$k\left(\mathbf{x}_{i},\mathbf{x}_{j}\right) = \sigma_{s}^{2} \left(1 + \sqrt{3}\sqrt{\sum_{m=1}^{4} \frac{\left(x_{im} - x_{jm}\right)^{2}}{I_{m}}}\right) exp\left(-\sqrt{3}\sqrt{\sum_{m=1}^{4} \frac{\left(x_{im} - x_{jm}\right)^{2}}{I_{m}}}\right) \left(5\right) \mathcal{N}\left(\begin{bmatrix}\mu\left(\mathbf{x}\right)\\\mu\left(\mathbf{x}^{*}\right)\end{bmatrix}, \begin{bmatrix}k\left(\mathbf{x},\mathbf{x}\right) & 0\\ 0 & k\left(\mathbf{x}^{*},\mathbf{x}^{*}\right)I\end{bmatrix}\right)$$

$$\epsilon (x) \sim \mathcal{N} (0, \sigma_n^2 (x) = c_6)$$
 (6)

resulting in a set of hyperparameters $\Theta = \{c_1, c_2, c_3, c_4, c_5, c_6, \sigma_s, l_1, l_2, l_3, l_4\}$. Within the prior mean hyperparameters $\{c_1, c_2, c_3, c_4, c_5\}$ are the slopes of the linear trend in the 4D of the parameter space and c_5 is the intercept.

Within the kernel function, the signal variance, σ_s , quantifies the epistemic uncertainty and the length scales, $\{I_1,I_2,I_3,I_4\}$, control the decay rate in covariance in each dimension. Finally, the noise function variance, with a hyperparameter c_6 , quantifies the data variability. These hyperparameters must be evaluated to fully characterize the GPR model to predict the *total score* at previously unseen points. This is usually done by estimating the values of the hyperparameters that maximize the log-likelihood of observing the data.

Bayesian Optimization: Efficiently exploring the parameter space requires carefully identifying experiments that lead to the maximum information gain about the halide perovskite. This is especially important given the many process parameters their complex interactions influencing the material properties. Traditional approaches rely on time-consuming, resource-intensive grid searches or random sampling methods. These methods frequently lead to inefficiencies in the exploration process, either by conducting insufficient experiments that result in inaccurate predictions or by performing excessive experiments that incur unnecessary costs. In this context, Bayesian optimization (BO) can intelligently navigate high-dimensional parameter spaces.

BO was used to efficiently explore and predict the total score at any point in the parameter space $X \subset \mathbb{R}^4$. BO has been implemented in several fields as an efficient approach to optimizing black-box functions relating process parameters to key performance measures. [24,47-49] In particular, this efficient approach is well-suited for perovskite optimization, as the experiments involved are expensive and time-consuming. BO is a sequential design approach composed of two key components: a probabilistic model, often a GPR model, to capture the current understanding of the perovskite total score as a function of the process parameters, and an acquisition function to guide the experimental process. The choice of the acquisition function depends on the BO objective. BO is mostly used for optimizing the parameter space, where the aim is to identify the value of the parameters that maximize the output of interest. For this purpose, studies often implement the Expected Improvement acquisition function, which balances the space exploration to escape local optima on the one hand, and space exploitation to quantify the global optima accurately on the other hand. [50] Another acquisition function is the upper confidence bound, which uses both predicted mean uncertainty from the GPR to identify the next set of experiments that maximize the output.^[51] While the objective of these functions is to maximize the output, the aim of our work is to efficiently explore the parameter space without focusing on one function property in particular. Here, the total correlation acquisition function was used to identify the points in the parameter space expected to maximize the information gained from the next experiments. Specifically, it identifies the new points in the parameter space x^* whose latent function values (predicted halide perovskite total score) are least correlated with each other, the total scores at the previously tested points x. Mathematically, the total correlation identifies x^* that minimizes the Kullback-Leibler (KL) divergence^[52] between two distributions. The first is the joint prior distribution of the noiseless function values at x and x^* with their correlation calculated by the kernel function. The second is the joint distribution of the noiseless function values, assuming that they are independent. This is illustrated using the following equation

$$KL (p (f (x), f (x^*)) || p (f (x)) .p (f (x^*))) = KL(A||B)$$
(7)

$$A \sim \mathcal{N}\left(\begin{bmatrix} \mu(\mathbf{x}) \\ \mu(\mathbf{x}^*) \end{bmatrix}, \begin{bmatrix} k(\mathbf{x}, \mathbf{x}) & k(\mathbf{x}, \mathbf{x}^*) \\ k(\mathbf{x}^*, \mathbf{x}) & k(\mathbf{x}^*, \mathbf{x}^*) \end{bmatrix}\right)$$
(8)

$$\frac{2}{k_{[5]}} \mathcal{N}\left(\begin{bmatrix} \mu(\mathbf{x}) \\ \mu(\mathbf{x}^*) \end{bmatrix}, \begin{bmatrix} k(\mathbf{x}, \mathbf{x}) & 0 \\ 0 & k_{[1}(\mathbf{x}^*)^*] \end{bmatrix}\right) \tag{9}$$

The aim is to identify x^* that minimizes this KL value, resulting in x^* that are the least correlated with each other and with x.

After performing experiments at the identified points and before updating the GPR model with the new data, the *total score* outliers in each batch (four samples synthesized at the same point in the parameter space) were identified and removed using the interquartile distance method. With this

www.advancedsciencenews.com



www.advenergymat.de

method, the *total score* values that lie above the 75th percentile or below the 25th percentile of the batch data by a distance of more than 1.5 the standard deviation are considered outliers. In addition, manual inspection of outcomes was done to exclude points where parts of the experiment did not proceed as expected.

SHAP Analysis: A Bayes Gaussian Process-based SHAP (BayesGPR-SHAP) analysis was conducted to assess the contribution of each synthesis condition to the total score, building on the stochastic SHAP value framework developed by Chau et al. for GPR models.^[29,53] In this study, an anisotropic Matérn kernel with v = 3/2 was employed to capture featurespecific correlations within the GPR, ensuring consistency with the GPR model used for optimization in this work. Unlike conventional deterministic SHAP methods, BayesGPR-SHAP accounts for both predictive uncertainty (from the GPR posterior) and estimation uncertainty (due to finite coalition sampling), providing more reliable uncertainty-aware feature attributions. This method enables the extraction of both local and global explanations, where local explanations break down the model's output at the individual data point level, identifying how each synthesis condition contributes to a specific prediction, while global explanations summarize feature importance by averaging the absolute local Shapley values across all data points, offering a comprehensive measure of each feature's overall influence. The more positive the SHAP values are, the higher the positive contribution to the total score (i.e., contributing to higher total scores). The more negative they are, the higher the negative contribution to the total score (i.e., contributing to lower total scores). For the global explanations, the mean absolute SHAP values indicate how important a specific feature contributes to the total score. The higher the values, the more important this feature is. From the bottom feature to the top feature, they are becoming more important to the total score.

Supporting Information

Supporting Information is available from the Wiley Online Library or from the author.

Acknowledgements

A.H. acknowledges the United States-India Educational Foundation (USIEF) for a Fulbright-Nehru Postdoctoral fellowship (Award No. 2978/ FNPDR /2023). D.-K.L. acknowledges the Office of Science, Office of Basic Energy Sciences, of the U.S. Department of Energy under Contract Number DE-SC-0023355. Work at the Molecular Foundry was supported by the Office of Science, Office of Basic Energy Sciences, of the U.S. Department of Energy under Contract No. DE-AC02-05CH11231. C.M.S.-F., M.B.A., Y.-R. Liu acknowledges support by the U.S. Department of Energy, Office of Science, Office of Basic Energy Sciences in the Early Career Research Program "Accelerated Robotic Design of Energy Materials (ACElab)". M.M.N. acknowledges the Center of Advanced Mathematics for Energy Research applications (CAMERA), funded by the U.S. Department of Energy, Office of Advanced Scientific Computing Research and Basic Energy Sciences under contract No. DE-AC02-05CH11231. S.S. acknowledges the startup fund and the Royalty Research Fund at the University of Washington. A.R.H. acknowledges the U.S. Department of Energy, Office of Science, Office of Workforce Development for Teachers and Scientists, Office of Science Graduate Student Research (SCGSR) program. The SCGSR program is administered by the Oak Ridge Institute for Science Education for the DOE under contract number DE-SC0014664. M.S.L. thanks the financial support from the National Science Foundation (ECCS award #2023974). S.A., C.M.S.-F. acknowledge funding from the Bavaria California Technology Center (BaCaTeC) Project No. 13 [2021-2].

Conflict of Interest

The authors declare no conflict of interest.

Author Contributions

A.H. and M.B.A. contributed equally to this work. S.A., E.B., and C.M.S.F. developed the initial robotic platform with further experimental additions by A.R., A.G., and A.H. Data management was supported by M.W., E.B., and N.T.A.H. and C.M.S.F. designed the experiment. M.B.A. integrated the BO/GPR algorithms. A.H. performed AutoBot and in situ PL experiments with the help of D.K.L. S.C., T.M.N., and S.S. developed the PL image metric and performed the SHAP analysis. The total score was developed by A.H., N.T., M.B.A., S.C., T.M.N., S.S., and C.M.S.F. Manual characterizations (XRD, SEM, and TRPL) were performed by A.H. D.K.L., Y.R.L., and M.M.N. helped with the revision. M.S.L. and C.M.S.F. supervised the experiments performed by A.R.H. C.M.S.F. and S.S. supervised the work and strategized the manuscript. C.M.S.F. and M.B.A. wrote the first manuscript revision. All the authors contributed to the discussion and manuscript revision.

Data Availability Statement

The data that support the findings of this study are available from the corresponding author upon reasonable request.

Keywords

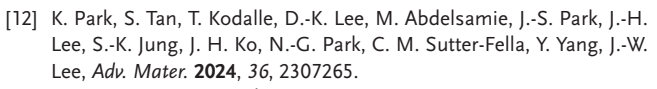
Al-Driven robot, closed-loop experiments, halide perovskites, machine learning, synthesis-property maps

Received: April 23, 2025 Revised: June 7, 2025 Published online: 16146840, 0, Downloaded from https://advanced.onlinelibrary.wiley.com/doi/10.1002/aemm.20250294 by University Of California - Davis, Wiley Online Library on [1607/2025]. See the Terms and Conditions (https://onlinelibrary.wiley.com/erms-ad-conditions) on Wiley Online Library for rules of use; OA arctics are governed by the applicable Ceravive Commons

- A. Aspuru-Guzik, K. Persson, Materials Acceleration Platform: Accelerating Advanced Energy Materials Discovery by Integrating High-Throughput Methods Artificial Intelligence 2018.
- [2] J. Wagner, C. G. Berger, X. Du, T. Stubhan, J. A. Hauch, C. J. Brabec, J. Mater. Sci. 2021, 56, 16422.
- [3] A. G. Kusne, H. Yu, C. Wu, H. Zhang, J. Hattrick-Simpers, B. DeCost, S. Sarker, C. Oses, C. Toher, S. Curtarolo, A. V. Davydov, R. Agarwal, L. A. Bendersky, M. Li, A. Mehta, I. Takeuchi, *Nat. Commun.* 2020, 11, 5066
- [4] M. M. Flores-Leonar, L. M. Mejía-Mendoza, A. Aguilar-Granda, B. Sanchez-Lengeling, H. Tribukait, C. Amador-Bedolla, A. Aspuru-Guzik, Curr. Opin. Green Sustain. Chem. 2020, 25, 100370.
- [5] N. J. Szymanski, B. Rendy, Y. Fei, R. E. Kumar, T. He, D. Milsted, M. J. McDermott, M. Gallant, E. D. Cubuk, A. Merchant, H. Kim, A. Jain, C. J. Bartel, K. Persson, Y. Zeng, G. Ceder, *Nature* 2023, 624, 86.
- [6] C. Wang, Y.-J. Kim, A. Vriza, R. Batra, A. Baskaran, N. Shan, N. Li, P. Darancet, L. Ward, Y. Liu, M. K. Y. Chan, S. K. R. S. Sankaranarayanan, H. C. Fry, C. S. Miller, H. Chan, J. Xu, Nat. Commun. 2025, 16, 1498.
- [7] J. Li, J. Li, R. Liu, Y. Tu, Y. Li, J. Cheng, T. He, X. Zhu, Nat. Commun. 2020, 11, 2046.
- [8] J.-P. Correa-Baena, K. Hippalgaonkar, J. van Duren, S. Jaffer, V. R. Chandrasekhar, V. Stevanovic, C. Wadia, S. Guha, T. Buonassisi, *Joule* 2018, 2, 1410.
- [9] J. Grizou, L. J. Points, A. Sharma, L. Cronin, *Sci. Adv.* **2020**, *6*, aay4237.
- [10] S. Langner, F. Häse, J. D. Perea, T. Stubhan, J. Hauch, L. M. Roch, T. Heumueller, A. Aspuru-Guzik, C. J. Brabec, Adv. Mater. 2020, 32, 1907801.
- [11] J. Zhang, B. Liu, Z. Liu, J. Wu, S. Arnold, H. Shi, T. Osterrieder, J. A. Hauch, Z. Wu, J. Luo, J. Wagner, C. G. Berger, T. Stubhan, F. Schmitt, K. Zhang, M. Sytnyk, T. Heumueller, C. M. Sutter-Fella, I. M. Peters, Y. Zhao, C. J. Brabec, Adv. Energy Mater. 2023, 13, 2370193.

on Wiley Online Library for rules of use; OA articles

are governed by the applicable Creative Commons



- [13] G. E. Eperon, S. N. Habisreutinger, T. Leijtens, B. J. Bruijnaers, J. J. van Franeker, D. W. deQuilettes, S. Pathak, R. J. Sutton, G. Grancini, D. S. Ginger, R. A. J. Janssen, A. Petrozza, H. J. Snaith, ACS Nano 2015, 9, 9380.
- [14] S. Pathak, A. Sepe, A. Sadhanala, F. Deschler, A. Haghighirad, N. Sakai, K. C. Goedel, S. D. Stranks, N. Noel, M. Price, S. Hüttner, N. A. Hawkins, R. H. Friend, U. Steiner, H. J. Snaith, ACS Nano 2015, 9, 2311
- [15] J.-W. Lee, S. Tan, S. I. Seok, Y. Yang, N.-G. Park, Science 2022, 375, abj1186.
- [16] S. Kundu, T. L. Kelly, Mater. Chem. Front. 2018, 2, 81.
- [17] N. Taherimakhsousi, M. Fievez, B. P. MacLeod, E. P. Booker, E. Fayard, M. Matheron, M. Manceau, S. Cros, S. Berson, C. P. Berlinguette, npj Comput. Mater. 2021, 7, 190.
- [18] K. M. Nandishwara, S. Cheng, P. Liu, H. Zhu, X. Guo, F. C. P. Massabuau, R. L. Z. Hoye, S. Sun, ChemRxiv. 2025, 1.
- [19] M. Yang, Z. Li, M. O. Reese, O. G. Reid, D. H. Kim, S. Siol, T. R. Klein, Y. Yan, J. J. Berry, M. F. A. M. van Hest, K. Zhu, *Nat. Energy* 2017, 2, 17038
- [20] D. N. Cakan, E. Oberholtz, K. Kaushal, S. P. Dunfield, D. P. Fenning, Mater. Adv. 2025, 6, 598.
- [21] A. Mannodi-Kanakkithodi, M. K. Y. Chan, J. Mater. Sci. 2022, 57, 10736
- [22] F. Akhundova, L. Lüer, A. Osvet, J. Hauch, I. M. Peters, K. Forberich, N. Li, C. Brabec, Appl. Phys. Lett. 2021, 118, 243903.
- [23] M. Ahmadi, M. Ziatdinov, Y. Zhou, E. A. Lass, S. V. Kalinin, *Joule* 2021, 5, 2797.
- [24] M. B. Alghalayini, D. Collins-Wildman, K. Higa, A. Guevara, V. Battaglia, M. M. Noack, S. J. Harris, Cell Rep. Phys. Sci. 2024, 6,
- [25] Z. Li, M. Yang, J.-S. Park, S.-H. Wei, J. J. Berry, K. Zhu, Chem. Mater. 2016, 28, 284.
- [26] D. P. McMeekin, G. Sadoughi, W. Rehman, G. E. Eperon, M. Saliba, M. T. Hörantner, A. Haghighirad, N. Sakai, L. Korte, B. Rech, M. B. Johnston, L. M. Herz, H. J. Snaith, *Science* 2016, 351, 151.
- [27] J. A. Aguiar, S. Wozny, T. G. Holesinger, T. Aoki, M. K. Patel, M. Yang, J. J. Berry, M. Al-Jassim, W. Zhou, K. Zhu, Energy Environ. Sci. 2016, 9, 2372.
- [28] V. L. Pool, B. Dou, D. G. Van Campen, T. R. Klein-Stockert, F. S. Barnes, S. E. Shaheen, M. I. Ahmad, M. F. A. M. van Hest, M. F. Toney, Nat. Commun. 2017, 8, 14075.
- [29] S. L. Chau, K. Muandet, D. Sejdinovic, Adv. Neural Inf. Process. Syst. 2023, 36, 50769.
- [30] S. L. Chau, R. Hu, J. González, D. Sejdinovic, Adv. Neural Inf. Process. Syst. 2022, 35, 13050.
- [31] S. Pratap, F. Babbe, N. S. Barchi, Z. Yuan, T. Luong, Z. Haber, T.-B. Song, J. L. Slack, C. V. Stan, N. Tamura, C. M. Sutter-Fella, P. Müller-Buschbaum, *Nat. Commun.* 2021, 12, 5624.

- [32] A. D. Taylor, Q. Sun, K. P. Goetz, Q. An, T. Schramm, Y. Hofstetter, M. Litterst, F. Paulus, Y. Vaynzof, Nat. Commun. 2021, 12, 1878
- [33] T. Kodalle, M. M. Byranvand, M. Goudreau, C. Das, R. Roy, M. Kot, S. Briesenick, M. Zohdi, M. Rai, N. Tamura, J. I. Flege, W. Hempel, C. M. Sutter-Fella, M. Saliba, Adv. Mater. 2024, 36, 2309154.
- [34] T.-B. Song, Z. Yuan, F. Babbe, D. P. Nenon, E. Aydin, S. De Wolf, C. M. Sutter-Fella, ACS Appl. Energy Mater. 2020, 3, 2386.
- [35] L. Bi, Q. Fu, Z. Zeng, Y. Wang, F. R. Lin, Y. Cheng, H.-L. Yip, S. W. Tsang, A. K.-Y. Jen, J. Am. Chem. Soc. 2023, 145, 5920.
- [36] H. Wang, Q. Li, Y. Zhu, X. Sui, X. Fan, M. Lin, Y. Shi, Y. Zheng, H. Yuan, Y. Zhou, H. Jin, H. G. Yang, Y. Hou, S. Yang, Energy Environ. Sci. 2025, 18, 2254.
- [37] B. G. H. M. Groeneveld, S. Adjokatse, O. Nazarenko, H.-H. Fang, G. R. Blake, G. Portale, H. Duim, G. H. ten Brink, M. V. Kovalenko, M. A. Loi, *Energy Technol.* 2020, 8, 1901041.
- [38] Z. Liang, Y. Zhang, H. Xu, W. Chen, B. Liu, J. Zhang, H. Zhang, Z. Wang, D.-H. Kang, J. Zeng, X. Gao, Q. Wang, H. Hu, H. Zhou, X. Cai, X. Tian, P. Reiss, B. Xu, T. Kirchartz, Z. Xiao, S. Dai, N.-G. Park, J. Ye, X. Pan, Nature 2023, 624, 557.
- [39] F. Zhang, M. Shao, C. Wang, W. Wen, W. Shi, M. Qin, H. Huang, X. Wei, Y. Guo, Y. Liu, Adv. Mater. 2024, 36, 2307326.
- [40] J. Kim, L. T. Schelhas, K. H. Stone, ACS Appl. Energy Mater. 2020, 3, 11269.
- [41] D. Zheng, T. Pauporté, J. Mater. Chem. A 2021, 9, 17801.
- [42] N. Li, J. Liu, C. Li, Y. Li, J. Jia, Y. Wu, H. Yu, B. Yuan, B. Cao, ACS Sustain. Chem. Eng. 2020, 8, 7020.
- [43] Y. Tian, I. G. Scheblykin, J. Phys. Chem. Lett. 2015, 6, 3466.
- [44] J. Mooney, P. Kambhampati, J. Phys. Chem. Lett. 2013, 4, 3316.
- [45] K. B. Lohmann, S. G. Motti, R. D. J. Oliver, A. J. Ramadan, H. C. Sansom, Q. Yuan, K. A. Elmestekawy, J. B. Patel, J. M. Ball, L. M. Herz, H. J. Snaith, M. B. Johnston, ACS Energy Lett. 2022, 7, 1903
- [46] J. Li, A. Dobrovolsky, A. Merdasa, E. L. Unger, I. G. Scheblykin, ACS Omega 2018, 3, 14494.
- [47] A. Hebbal, L. Brevault, M. Balesdent, E.-G. Talbi, N. Melab, Optim. Eng. 2021, 22, 321.
- [48] W. Li, J. Hu, Z. Chen, H. Jiang, J. Wu, X. Meng, X. Fang, J. Lin, X. Ma, T. Yang, P. Cheng, R. Xie, Sol. Energy 2023, 262, 111853.
- [49] Z. Liu, N. Rolston, A. C. Flick, T. W. Colburn, Z. Ren, R. H. Dauskardt, T. Buonassisi, Joule 2022, 6, 834.
- [50] C. Qin, D. Klabjan, D. Russo, Adv. Neural Inf. Process. Syst. 2017, 30,
- [51] N. Srinivas, A. Krause, S. M. Kakade, M. W. Seeger, *IEEE Trans. Inf. Theory* 2012, 58, 3250.
- [52] S. Kullback, Information Theory Statistics, Courier Corporation, United States, 1997.
- [53] Eds.: S. Koyejo, S. Mohamed, A. Agarwal, D. Belgrave, K. Cho, A. Oh, 35: Annual Conference on Neural Information Processing Systems, New Orleans, LA, USA, November – December, 2022.